

Biowaste Orange Peel-Derived Mesoporous Carbon as a Cost-Effective Anode Material with Ultra-Stable Cyclability for Potassium-Ion Batteries

Rakesh Verma,^[a] Yashabanta N. Singhbabu,^[a] Pravin N. Didwal,^[a] An-Giang Nguyen,^[a] Jaekook Kim,^[a] and Chan-Jin Park^{*[a]}

Potassium-ion batteries (PIBs) are promising alternative to Lithium-ion batteries (LIBs) owing to their economic merits. However, the PIBs have not met suitable anode materials comparable to graphite in LIBs. We synthesised an orange peel-derived mesoporous carbon (OPDMC) as a potential anode material for high performance PIBs via facile one-step carbonisation with self-activation from waste orange peel. The OPDMC-1000, which were carbonised at 1000 °C, exhibited impressive initial discharge/charge capacities of

408/224 mAh g⁻¹ at 30 mA g⁻¹ and retained the reversible capacity of 208.57 mAh g⁻¹ over 100 cycles. Even after 2000 and 3000 cycles at specific currents of 200 and 500 mA g⁻¹, it maintained the reversible capacities of 150.37 and 112 mAh g⁻¹, respectively. A full cell employing the OPDMC exhibited an initial reversible discharge capacity of 185.32 mAh g⁻¹ at 50 mA g⁻¹ with capacity retention of 71.60% after 50 cycles, indicating its practical applicability.

1. Introduction

Li-ion batteries (LIBs), which have a high energy density and outstanding cyclability, have dominated the commercial market for the past two decades, particularly in portable electronic devices and electric vehicles.^[1,2] Nonetheless, the increasing energy needs, limited Li resources, and uneven distribution of Li are serious concerns.^[3] Therefore, investigating alternatives to LIBs with low cost, availability, and safety is imperative. In this regard, different metal-ion batteries, such as Al-, Mg-, Na-, and K-ion batteries, are under active consideration.^[4–7]

K-ion batteries (PIBs) and Na-ion batteries (SIBs) as promising alternatives to LIBs owing to their low costs, high ionic conductivity, and high cell potential.^[8,9] Among these two types of batteries, more attention should be paid to PIBs for the development of low-cost and high-energy density PIBs, for the following reasons.^[10] (1) The natural abundance of K (2.09 wt.%) is 1000 times higher than that of Li (0.0017 wt.%) and comparable to that of Na (2.36 wt.%).^[11] (2) The redox potential of K⁺/K (−2.97 V vs. SHE) is lower than that of Na⁺/Na (−2.71 V vs. SHE) but very close to that of Li⁺/Li: −3.04 V vs. SHE), signifying a higher working voltage and energy density for PIBs compared with SIBs.^[12] (3) Al can be used as the current collector instead of Cu, in contrast to the case of LIBs, eliminating the formation of K-Al alloys at a low potential,

which is useful for commodity cells with a high energy density and reduced fabrication cost.^[13] In addition, K-based dual ion batteries have to pay much attention due to their high potential, low cost, and environmental friendliness.^[14–17]

In research based on the mechanism of K-ion storage, three potential anode materials are under active consideration; carbonaceous, alloy-based, and conversion-based materials.^[18] The large volume changes during potassiation and depotassiation are the main disadvantage of the alloy- and conversion-based materials.^[19–22] In contrary, carbonaceous materials are among the best potential anodes owing to their good conductivity and high thermal stability. Carbonaceous materials such as hard carbon, graphene, carbon nanotubes, and graphite have been investigated as anode materials for PIBs.^[23–26] However, the large ionic radius of the K⁺ ion leads to a large volume change and low rate of K⁺ ion diffusion during the potassiation process, resulting in poor cycling performance and poor rate performance of the anode for PIBs.^[27] To address this issue, recent studies have focused on the synthesis of a porous structure with large interlayer spacing,^[28] as well as doping with heteroatoms,^[29–31] to reduce the volume change and increase the K⁺ ion diffusion rate. Among these methods, optimizing the porous morphology of carbonaceous materials is suitable and vital to accommodate volume expansion and enhance the K⁺ ion diffusion rate during cycling for achieving a high-performance anode.^[32,33] Thus, developing an efficient, ecofriendly, and effective technique for synthesizing porous-structure and large-interlayer spacing carbonaceous materials is of immense importance.

Recently, porous carbonaceous materials derived from biomass, such as potato, skimmed cotton, waste-tire rubber, and walnut septum, have been investigated as anode materials have been used for PIBs.^[34–37] Biomass-derived carbon has the following advantages: it is renewable and cost-effective and

[a] Dr. R. Verma, Dr. Y. N. Singhbabu, P. N. Didwal, A.-G. Nguyen, Prof. J. Kim, Prof. C.-J. Park
Department of Materials Science and Engineering
Chonnam National University
77, Yongbongro, Bukgu, Gwangju 61186, South Korea
Fax: + (82)-62-530-1699
E-mail: parkcj@jnu.ac.kr

 Supporting information for this article is available on the WWW under
<https://doi.org/10.1002/batt.202000068>

can provide an attractive three-dimensional (3D) porous nanostructure, which is beneficial for a high storage capacity and good cyclic performance in batteries.^[38] However, in most cases, chemical activating agents such as KOH, NaOH, and ZnCl₂ are used to produce porous carbon via carbonisation.^[39] Subsequently, the used inorganic metallic components from the porous carbon must be removed, which not only adds an extra step but also increases the cost of production. Therefore, it is important to find a suitable biomass capable of producing porous carbon via simple carbonisation without the use of an activating agent. Orange peel (OP) appears to be applicable for this purpose. Furthermore, 15.6 million tons of OP are discarded every year.^[40] OP, which accounts for half of the total weight of orange fruits, is generally discarded, and some compounds released from the waste, such as phenols, can cause soil pollution.^[41] Therefore, Biowaste of orange peel (OP) is one of soil pollution problems. It would be highly beneficial to use OP waste as a resource for an electrode for batteries. Nevertheless, few studies have been performed on the use of OP powder carbonised via chemical activation for supercapacitor applications.^[42,43] Additionally, no studies have been performed on the 3D interconnected mesoporous design of OP-derived carbon via a self-activation process and its application as an anode in PIBs.

In this study, we used OP (skin of *Citrus sinensis*, family of Rutaceae) as a cost-effective precursor to fabricate 3D interconnected, OP-derived mesoporous carbon (OPDMC). The OPDMC was synthesised through a facile one-step carbonisation approach without introducing an activation agent, and pores were generated via a self-activation process. The self-activation process used the gases emitted during the carbonisation of the biowaste OP to produce pores in the carbon network, in contrast to chemical activation or physical activation. Therefore, compared with the chemical and physical activation approaches, the self-activation process is more ecofriendly and cost-effective. This cost-effective precursor and facile one-step synthesis method would be beneficial for the large-scale production of OPDMC. The OPDMC, which were heat-treated at 1000 °C, exhibited a superior rate performance and ultrahigh cycling stability over 3000 cycles at a specific current of 500 mAg⁻¹, with a columbic efficiency close to 100%. Furthermore, a full cell exhibited an impressive reversible charge capacity of 227 mAh g⁻¹ in the initial cycle and a capacity retention of 71.6% after 50 cycles.

2. Results and Discussion

2.1. Structural and Morphological Characterisation of OPDMC

The synthesis of the mesoporous carbon derived from the biowaste orange peel (OP) is graphically presented in Scheme 1. The biowaste OP was washed, dried, and ground into power. The mesoporous carbon was synthesised via a simple single-step carbonisation process at various temperatures (500, 700, and 1000 °C) in an Ar environment in a vertical furnace, using biowaste OP powder as a carbon precursor. To



Scheme 1. Procedure for the synthesis of orange peel-derived mesoporous carbon (OPDMC).

investigate the nature of the carbonaceous material formed by heating the OP powder in the Ar atmosphere and the effects of the heating temperature on the structure and morphology, the detailed structural, morphological, and microstructural characterisations were performed. The final obtained OPDMCs are denoted as OPDMC-500, OPDMC-700, and OPDMC-1000, corresponding to the carbonisation temperatures of 500, 700, and 1000 °C, respectively. Figure 1a shows the XRD patterns of OPDMC samples synthesised at different temperatures. All the samples exhibited two broad peaks around 23.4° and 43.6°. Such broad peaks in an XRD pattern are observed in three cases: (1) amorphous carbon, (2) graphene derivatives (two-dimensional (2D) carbonaceous materials), and (3) turbostratic carbon which is an intermediate structure between amorphous and crystalline carbon. In the case of amorphous carbon, only one broad peak appears at 18–20°, whereas for carbonaceous 2D materials, two peaks appear at 26° and 45°. In the case of turbostratic carbon, a broad peak appears between 21° and 25°. In our case, the broad peaks appeared at 23.4°. This 2θ value is between those of amorphous carbon and carbonaceous 2D materials; therefore, the carbonaceous material obtained by heating the OP was turbostratic in nature, and the structure comprised a mixture of crystalline and amorphous domains. This was verified via TEM, as discussed in the next section. Hence, the two broad peaks at 23.4° and 43.6° are attributed to the (002) and (101) crystallographic planes, respectively, of turbostratic carbon. With the increasing carbonisation temperature, the peak intensity increased, owing to the improvement of the structural ordering. The interlayer spacing (*d*) for the (002) plane was calculated using Bragg's equation, and the values are presented in Table S1 (Supporting Information). As shown, the *d* values were similar for all the OPDMC samples. For the OPDMC-1000 sample, the *d* value was 0.379 nm, which is higher than that of graphite.

To confirm the turbostratic nature of the synthesised carbon, Raman characterisation was performed. Figure 1b shows the Raman spectra of the OPDMC samples. In all cases, the characteristic D and G bands appeared at 1350 and 1585 cm⁻¹, respectively, with a broad hump in the 2D region. A careful observation of the Raman spectra revealed that for the OPDMC-500 and OPDMC-700 samples, the G-peak had a higher

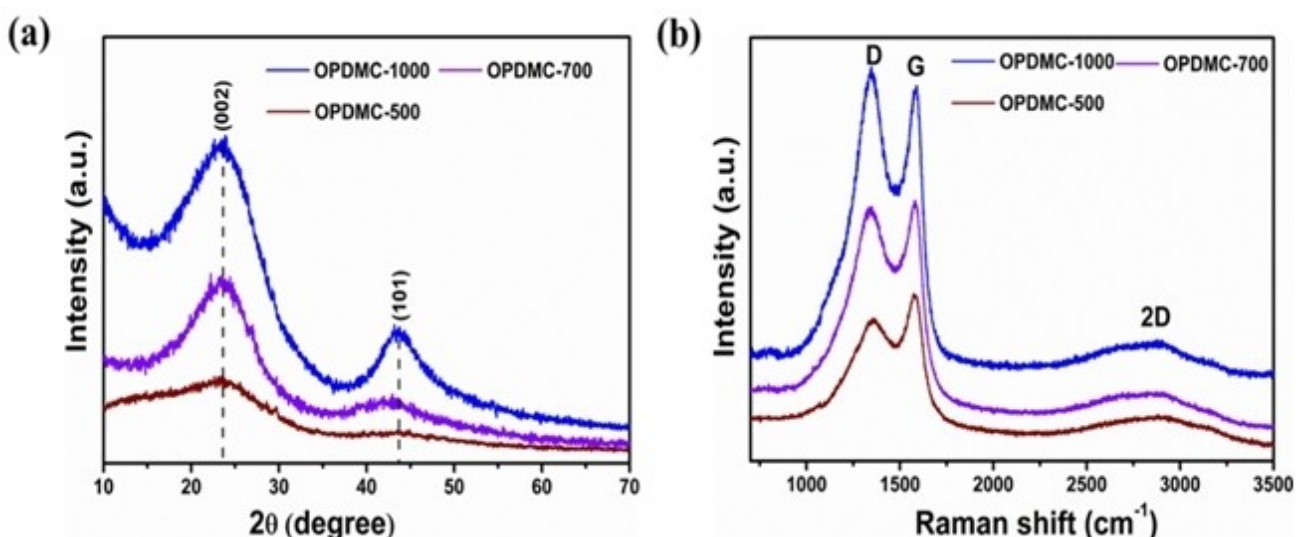


Figure 1. a) XRD patterns and b) Raman spectra of the OPDMC-1000, OPDMC-700, and OPDMC-500 samples.

intensity than the D-peak, and the opposite trend was observed for the OPDMC-1000 sample. This was verified by the I_D/I_G ratio, as shown in Table S1 (Supporting Information); for the OPDMC-500 and OPDMC-700 samples, the I_D/I_G ratio was < 1 , whereas for the OPDMC-1000 sample, it was > 1 . This observation can be explained as follows: as the temperature increased, more sp^2 domains were formed around defects, and thus the intensity of the D-peak increased with the carbonisation temperature. Similar observations were well documented in the literature.^[44,45]

To further investigate the elemental composition of the OPDMC, C/O ratio, residual O-containing functional groups, and effect of the temperature on the stability of the O functionalities, XPS analysis was performed. Figure 2a presents the survey XPS spectra of the OPDMC samples heated at 1000, 700, and 500 °C, which comprised only the elements C and O. Most importantly, the intensity of the O1s peak decreased with increasing temperature. This indicates the removal of O-containing functional groups with increasing temperature. To elucidate the extent of the reduction, the C/O ratio was calculated. As shown in Table S1 (Supporting Information), the C/O ratio at 500 °C was 2.5, and it increased to 13 when the temperature was increased to 1000 °C, indicating the significant reduction of O-containing functional groups at higher temperatures. Furthermore, to investigate the extent of the reduction, the nature of the O-containing functional groups, and their percentage, the high-resolution C1s peak was analysed using the CASA XPS software. Figure 2(b,d) show the deconvoluted C1s spectrum of the OPDMC-1000, OPDMC-700, and OPDMC-500 samples, respectively. For OPDMC-500 and OPDMC-700, the C1s spectrum was broad, whereas for OPDMC-1000, it was relatively sharper. The C1s spectrum of the OPDMC-500 sample was deconvoluted into five peaks at binding energies of 284.6, 285.6, 286.5, 287.5, and 288.8 eV, corresponding to C=C/C–C, alcohol/phenol, epoxy, carbonyl, and carboxyl functional groups, respectively. However, for the OPDMC-700 sample, the

spectrum was deconvoluted into only four peaks, corresponding to C=C/C–C, phenol, carbonyl, and carboxyl functional groups. At 700 °C, the alcohol and epoxy groups were not stable and hence were completely reduced. For the OPDMC-1000, the spectrum also contained four peaks, but the intensity of the O-containing functional groups (carbonyl and carboxyl groups) decreased significantly, indicating that these functionalities were based on abundant sp^2 -bonded carbon atoms. The percentages of these functional groups in the OPDMC samples are presented in Table S1 (Supporting Information). As shown, for the sample heated at 500 °C, C=C/C–C, alcohol/phenol, epoxy, carbonyl, and carboxyl functional groups were present in concentrations of 68%, 16%, 6%, 4%, and 6%, respectively. For the sample heated at 700 °C, C=C/C–C, phenol, carbonyl, and carboxyl functional groups were present in concentrations of 69%, 19%, 8%, and 4%, respectively, and for the sample heated at 1000 °C, the concentrations were 72%, 21%, 4%, and 3%, respectively. These observations indicate that for the sample heated at 1000 °C, the proportion of sp^2 -bonded C atoms was 93% (C=C/C–C + phenol –OH), and the sp^3 network accounted for only 7%. The results suggest that the OPDMC-1000 sample had better electronic conductivity than the other samples because of the larger amount of the sp^2 network.

After verifying the nature of the carbonaceous material formed from the OP via heating, we examined the morphology of the OPDMC using SEM. SEM images of the OPDMC samples are shown in Figure 3. The OPDMC-1000 (Figure 3a) sample exhibited 3D interconnected porous networks and a smooth surface. The formation of this porous structure can be explained as follows. Biowaste OP is mainly composed of cellulose, hemicellulose, lignin, pectin, and chlorophyll pigments. During carbonisation, these components of the biowaste OP gradually decomposed, leading to the release of CO, H₂, CO₂, and CH₄ gases, which produced the porous structure. Further, the 3D interconnected porous networks were not well-defined and appeared blocked for the OPDMC-700 (Figure 3c)

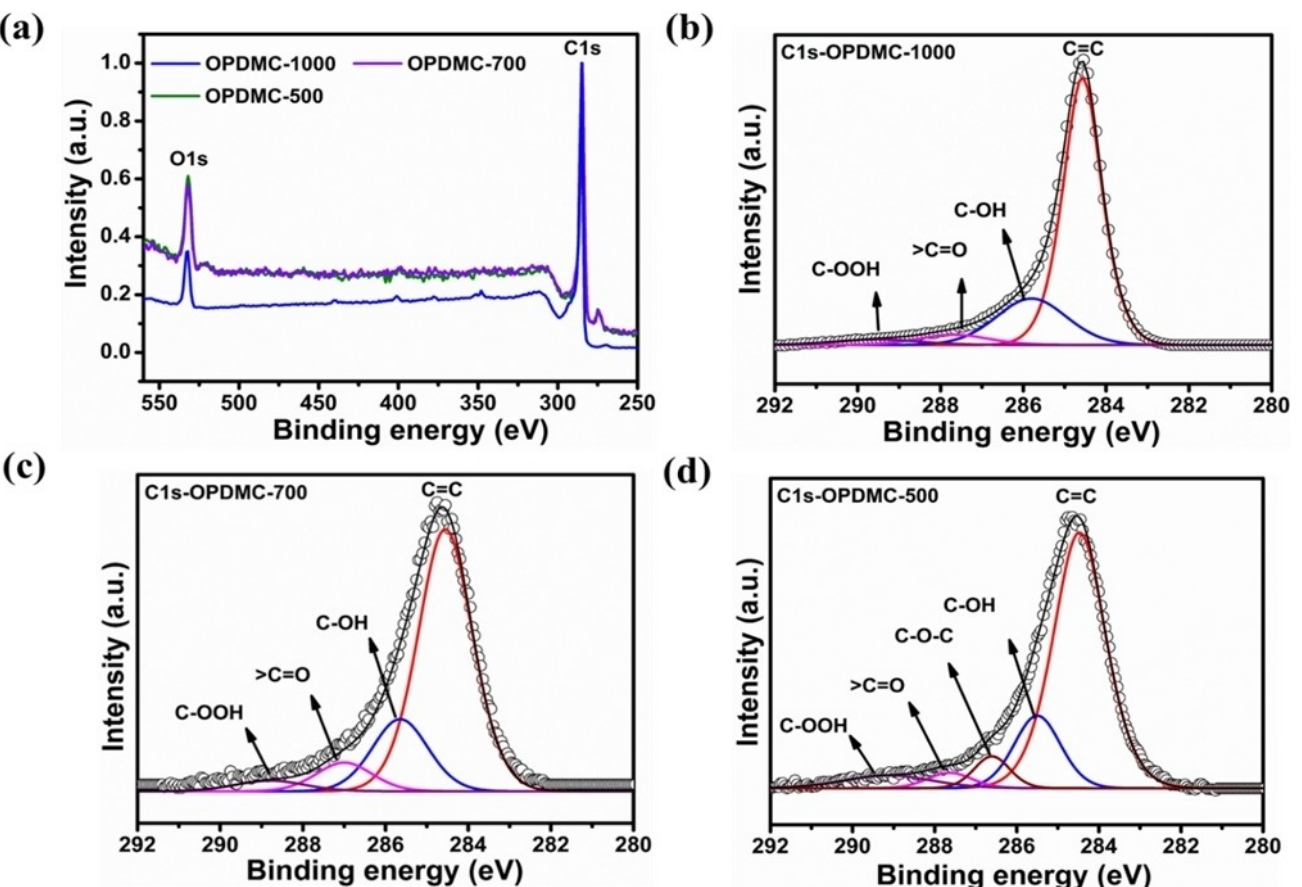


Figure 2. XPS spectra of the OPDMC samples. a) Survey spectra of OPDMC-1000, OPDMC-700, and OPDMC-500; b–d) deconvoluted C1s high-resolution spectra of OPDMC-1000, OPDMC-700, and OPDMC-500.

and d) and OPDMC-500 (Figure 3e and f) samples owing to the insufficient carbonisation temperature, which led to less gas evolution. The microstructure of the OPDMC-1000 sample was further characterised using high-resolution TEM (HRTEM). Figures 4a and b show the carbon sheets with a crumbled and wrinkled morphology. The mesoporous carbon had a size of approximately 10–15 nm. Figure 4c shows the localised graphite sheets, which are known as a turbostratic carbon structure. Further, the inset of Figure 4c shows the selected-area electron diffraction (SAED) pattern, which indicates the crystallinity due to the turbostratic layering of carbon, as confirmed by the XRD results. It is expected that such structure will provide additional K-ion storage sites, resulting in the high specific capacity.

The surface area and porosity significantly affect the electrochemical properties. Therefore, the surface area and pore-size distribution were investigated via the Brunauer–Emmett–Teller (BET) and Barrett–Joyner–Halenda (BJH) methods, respectively. The N₂ adsorption–desorption isotherms and pore-size distributions of the OPDMC samples are shown in Figure 5 and Figure S1 (Supporting Information). The specific surface area of the OPDMC increased with the carbonisation temperature, owing to the formation of the mesoporous structure. The specific surface area was 64.25, 3.95, and 1.80 m² g⁻¹ for OPDMC-1000, OPDMC-700, and OPDMC-500, respectively, and the corresponding pore volumes were 0.0349, 0.0067, and

0.0085 cm³ g⁻¹, respectively. With the increasing carbonisation temperature, the pores of OPDMC-1000 were homogeneously centred at 2.45 nm (Figure 5b), whereas the OPDMC-700 and OPDMC-500 samples exhibited irregular pore-size distributions, as shown in Figure S1 (Supporting Information). This indicates that the OPDMC-1000 sample subjected to the high-temperature carbonisation well maintained its homogeneous mesoporous structure. After the morphological and microstructural investigations of the OP-derived carbonaceous materials, we examined the electrochemical properties of the samples as anodes for PIBs.

2.2. Electrochemical Characterisation of OPDMC

The electrochemical properties of the OPDMC samples were evaluated by obtaining the cyclic voltammetry (CV) and galvanostatic discharge/charge potential profiles. According to these properties, the best sample with regard to the K-storage capability of the OPDMC was identified, and a detailed electrochemical-property evaluation was conducted for the best sample. Figure 6a presents the cyclic voltammograms of OPDMC-1000 in the potential range 0.01–2.0 V vs. K/K⁺, which were obtained at a scan rate of 0.1 mV s⁻¹. During the first cycle cathodic scan, a reduction peak appeared at 0.82 V vs. K/K⁺,

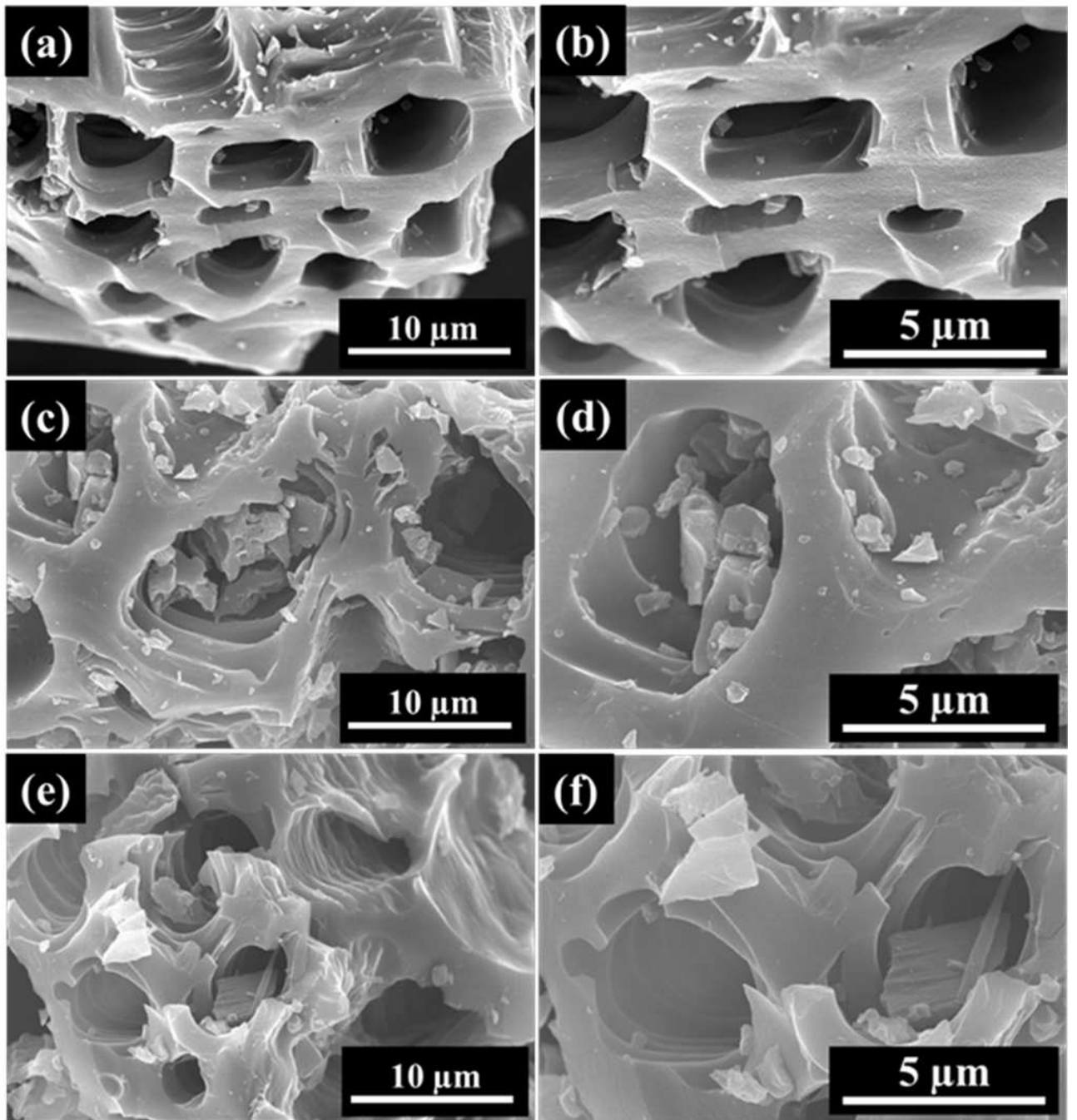


Figure 3. Low- and high-magnification SEM images: a, b) OPDMC-1000; c, d) OPDMC-700; e, f) OPDMC-500.

which was absent in the subsequent cycles, indicating the formation of a solid-electrolyte interphase (SEI) layer due to the decomposition of the electrolyte.^[46] The slightly humped peak at 0.52 V vs. K/K⁺ confirmed the presence of a slopping plateau in the galvanostatic discharge/charge cycles (Figure 6b). Additionally, a sharp reduction peak appeared at 0.01 V vs. K/K⁺, indicating the insertion of K-ions into the mesoporous carbon, which formed the K-intercalated compound.^[24,37] During the anodic scan, an oxidation peak appeared at ~0.35 V vs. K/K⁺, indicating the depotassiation of the mesoporous carbon.^[46,47] The slightly humped peak at 0.98 V vs. K/K⁺ indicates the

presence of a slopping plateau in the galvanostatic discharge/charge cycles (Figure 6b). Furthermore, from the second cycle onward, all the reduction and oxidation peaks almost overlapped each other, indicating the excellent cycling stability.

The selected galvanostatic discharge/charge potential profiles for the 1st, 2nd, 3rd, and 10th cycles of the OPDMC-1000 electrode are shown in Figure 6b, and those for OPDMC-700 and OPDMC-500 are shown in Figure S2 (Supporting Information). The OPDMC-1000 electrode exhibited an initial discharge capacity of 408 mAh g⁻¹ and a reversible charge capacity of 224 mAh g⁻¹, which were significantly higher than those of the

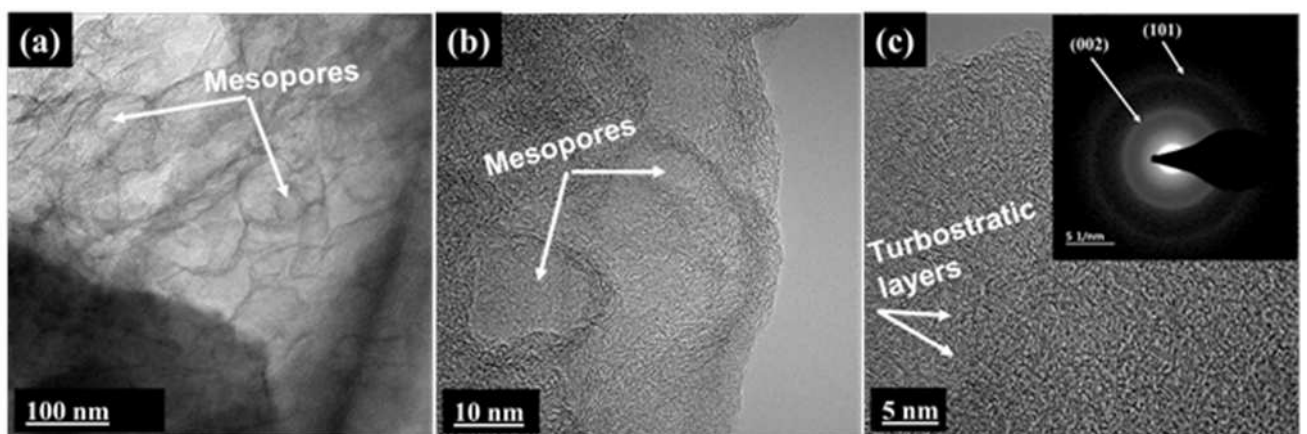


Figure 4. TEM images of OPDMC-1000. a) TEM image; b, c) HRTEM images. The inset in (c) shows the SAED pattern.

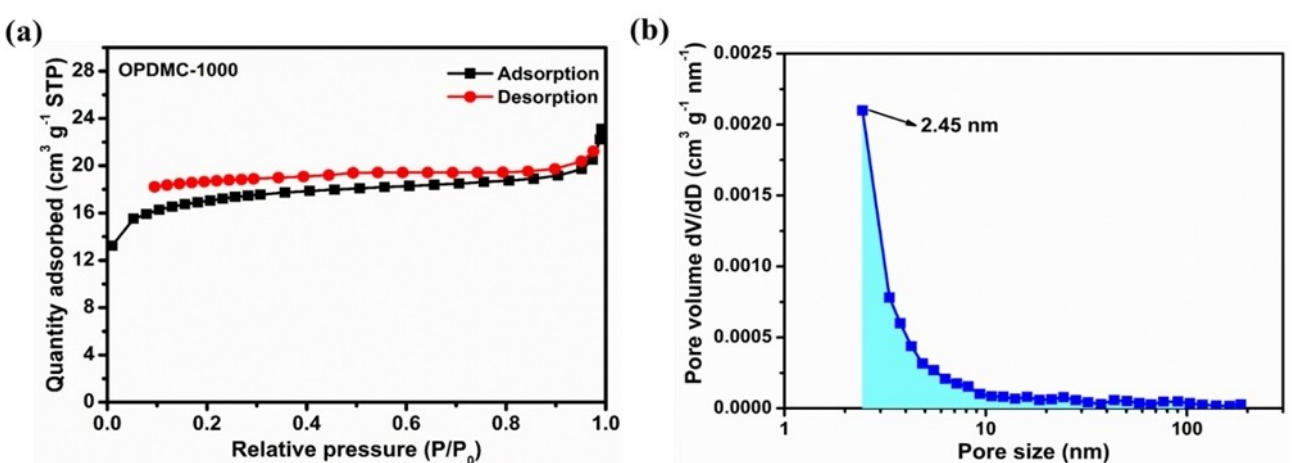


Figure 5. BET analysis results for OPDMC-1000. a) N_2 adsorption-desorption isotherm; b) BJH plot of the pore-size distribution.

OPDMC-700 electrode (404 and 194 mAh g⁻¹) and the OPDMC-500 electrode (397.8 and 125.68 mAh g⁻¹). Additionally, the OPDMC-1000 electrode exhibited a higher initial coulombic efficiency (55%) than OPDMC-700 (48%) and OPDMC-500 (31.6%). The initial irreversible capacity was due to the formation of the SEI layer on the surface of the OPDMC electrode during the first cycle.^[48,49] Subsequently, the coulombic efficiency gradually increased and stabilised with increasing cycles, indicating that the SEI layer was mainly formed in the first discharge cycle. Figure 6c displays the cyclability of the OPDMC-1000, OPDMC-700, and OPDMC-500 electrodes at a specific current of 30 mA g⁻¹. The first-cycle reversible specific capacities of the OPDMC-1000, OPDMC-700, and OPDMC-500 electrodes were 224, 194, and 125.68 mAh g⁻¹, respectively. After 100 cycles, the OPDMC-1000, OPDMC-700, and OPDMC-500 electrodes retained the capacities of 208.57, 145.7, and 90 mAh g⁻¹, respectively. These results indicate that as the heating temperature increased, the K-storage capacity of the OPDMC-1000 electrodes increased.

The improvement of the specific capacity with the increase in the temperature is attributed to the synergistic effects of the

enhancement in the electrical conductivity, the presence of O-containing functional groups, and the evolution of the porous structure. Indeed, the XRD results indicated that as the carbonisation temperature increased, the structural ordering was improved (Figure 1a). Further, the XPS results indicated that the proportion of the sp^2 network increased significantly with an increase in the carbonisation temperature (Table S1, Supporting Information). Additionally, the BET study revealed the presence of a well-defined porous structure with 3D interconnected pores for the sample heated at 1000 °C, with larger pore volumes compared with the samples heated at 700 and 500 °C. Therefore, the OPDMC-1000 sample had a higher electrical conductivity owing to the improved ordering and the presence of more sp^2 domains. Furthermore, the well-defined 3D interconnected pores with a larger pore volume facilitated the ion transfer, accommodated more K-ions, and suppressed the volume expansion more effectively compared with the OPDMC-500 and OPDMC-700 electrodes. Although the OPDMC-500 sample contained more O-containing functional groups than the other samples, it exhibited poor electrochemical performance. This is attributed to the lower electrical con-

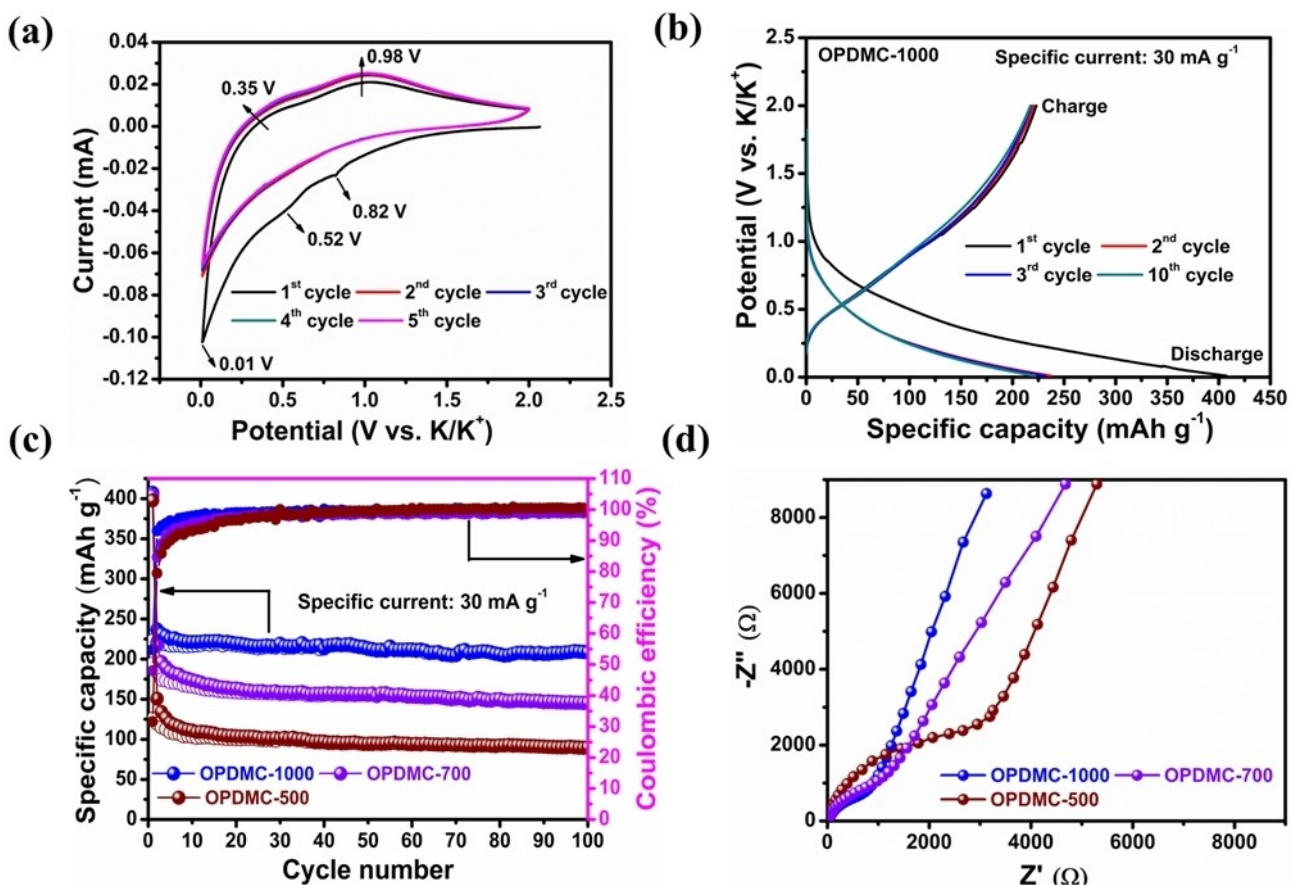


Figure 6. Electrochemical performance of OPDMC electrodes at 30 °C; a) cyclic voltammograms of the OPDMC-1000 electrode at 0.1 mVs⁻¹. b) Galvanostatic discharge/charge potential profiles of OPDMC-1000 at 30 mA g⁻¹. c) Cyclability of OPDMC-1000, OPDMC-700, and OPDMC-500 at 30 mA g⁻¹. d) Electrochemical impedance spectra of OPDMC-1000, OPDMC-700, and OPDMC-500.

ductivity and non-uniform pore distribution, which led to poor kinetics. Therefore, the enhanced K-ion storage capability of OPDMC-1000 is attributed to the combined effects of the electrical conductivity, presence of O-containing functionalities, and well-defined 3D interconnected pores.

The kinetics of the OPDMC electrodes before the cycling tests were compared according to the electrochemical impedance spectroscopy (EIS) curves, as shown in Figure 6d. The typical result of one semicircle in the middle-to-high frequency range with a sloping straight line at a low frequency was observed in all cases. The radius of the semicircle decreased with an increase in the carbonisation temperature. This indicates that the charge-transfer resistance was the lowest for the OPDMC-1000 anode. The EIS results corroborate our claims regarding the reasons for the better electrochemical performance of the OPDMC-1000 electrode. All the electrochemical characterisations suggest that OPDMC-1000 was superior to OPDMC-700 and OPDMC-500 for K-ion storage. Therefore, the rate performance of the OPDMC-1000 anode was evaluated to examine its behaviours at higher rates.

Figure 7a shows the initial discharge/charge curves of the OPDMC-1000 electrode at various specific current ranging from 25 to 1000 mA g⁻¹. Even when the specific current increased leading to the increase in cell polarisation, the overall shapes of

the discharge/charge potential profiles were similar, indicating the excellent stability of the OPDMC-1000 electrode. Further, at various specific currents, the OPDMC-1000 electrode exhibited excellent rate performance and long-term cycle stability. As shown in Figure 7b, the OPDMC-1000 electrode delivered reversible discharge specific capacities of 426.94, 209.94, 185.20, 166.83, 148.40, 123.33, and 101.50 mA g⁻¹ at specific currents of 25, 50, 100, 200, 300, 500, and 1000 mA g⁻¹, respectively, which are all higher than those of the OPDMC-700 and OPDMC-500 electrodes (Figure S3, Supporting Information). Moreover, the capacity recovered when the specific current was reversed to 25 mA g⁻¹, indicating that the OPDMC-1000 electrode had superior reversibility.

Further, we tested the long-term cycling performance of the OPDMC-1000 electrode at high specific currents of 200 and 500 mA g⁻¹ (Figure 7c and d). As expected, it exhibited impressive cycling stability, maintaining reversible capacities of 150.37 and 112 mA g⁻¹ after 2000 and 3000 cycles, respectively, which corresponds to a coulombic efficiency of near 100%. Interestingly, when tested at 1000 mA g⁻¹, the OPDMC-1000 electrode delivered reversible discharge capacity of 145.2 mA g⁻¹ with capacity retention of 68% and a coulombic efficiency of 99.6% after 500 cycles, as presented in Figure S4a and b (Supporting Information). Moreover, the electrochemical

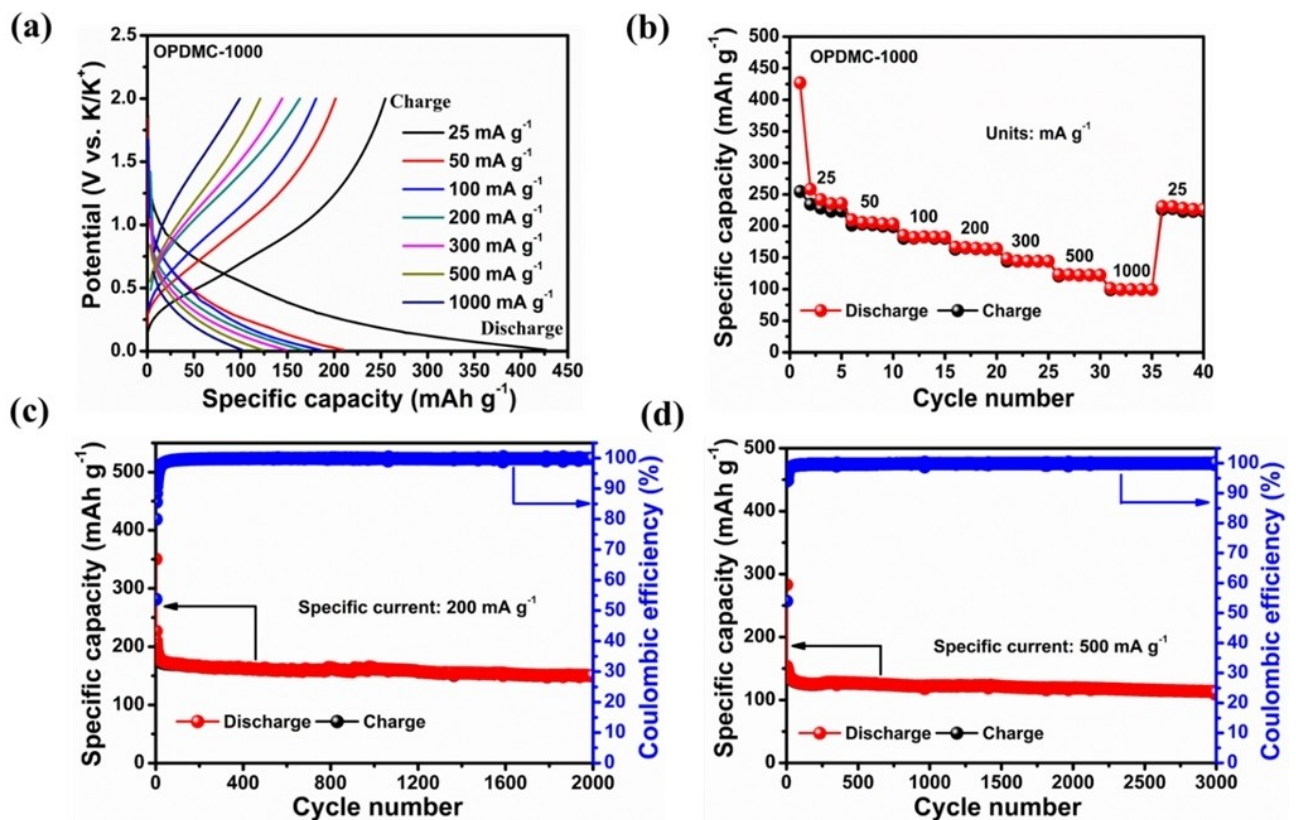


Figure 7. a) Galvanostatic discharge/charge potential profiles at various specific currents. b) Rate capability of the OPDMC-1000 anode at various specific currents ranging from 25 to 1000 mA g⁻¹. c, d) Long-term cycling performance of the OPDMC-1000 electrode at high specific currents of 200 mA g⁻¹ for 2000 cycles and 500 mA g⁻¹ for 3000 cycles, respectively.

performance of our OPDMC-1000 electrode was compared with porous carbon based anodes, which was previously reported in literature, as shown in the Table 1. (Supporting Information).

The excellent rate capability and long-term cycling performance of the OPDMC-1000 electrode were mainly due to the unique 3D interconnected micropore structure, large interlayer

Table 1. Comparison of electrochemical performance of the OPDMC-1000 electrode with reported porous carbon based anodes in PIBs.

Materials	Specific current [mA g ⁻¹]	Reversible discharge capacity [mAh g ⁻¹]	Cycles number	Capacity retention [mAh g ⁻¹]	Ref.
OPDMC-1000	30	236	100	208.57	This work
	200	226.51	2000	150.37	
	500	153.58	3000	112	
Reduced graphene oxide	10	~190	175	150	[58]
Graphite	20	~240	100	140	[59]
N-doped rich hard carbon	33	~240	200	205	[60]
Graphitic carbon nanocage	55	~230	100	195	[61]
Few-layer graphene	100	~245	100	140	[62]
Waste-tire derived carbon	140	~285	200	155	[36]
Bacterial-derived hierarchical porous carbon	200	~210	100	168	[63]
	500	~199	500	156	
Hierarchical porous carbon	50	~275	50	211	[64]
	1000	~180	1000	90.1	
N-doped carbon derived from walnut septum	100	263.6	200	242.5	[37]
	1000	~230	1000	119.9	
S/O co-doped porous carbon	50	~280	100	226.6	[30]
	1000	~210	2000	108	
F-doped graphene	50	~320	200	165.9	[24]
N/O doped hard carbon	50	315	100	230	[65]
Potato derived biomass porous carbon	100	~273	100	247.8	[34]
	500	~200	400	196	
Mesoporous carbon	50	~375	100	~250	[50]
	1000	~170	1000	146	

spacing, presence of more sp^2 domains, and large surface area compared with those of OPDMC-700 and OPDMC-500 electrodes.

2.3. K-Ion Storage Mechanism of OPDMC

To understand the K-ion insertion/desertion mechanism of the OPDMC-1000 electrode, XRD, TEM, XPS, and Raman spectroscopy analyses were performed after the coin cells were disassembled in the fully discharged and charged states. Figure S5 (Supporting Information) shows the XRD patterns of the OPDMC-1000 electrodes before and after it was discharged to 0.01 V vs. K/K^+ . The XRD pattern of the OPDMC-1000 pristine electrode exhibited a broad peak at $2\theta \approx 23.4^\circ$, with an interlayer distance of 0.38 nm. After the potassiation process through complete discharging to 0.01 V vs. K/K^+ , the XRD pattern was completely different from that of the pristine electrode, with the appearance of sharp diffraction peaks. Furthermore, the peak corresponding to the (002) plane shifted to a lower 2θ value after potassiation. The analysis of these sharp peaks confirms the formation of the KC_8 (JCPDS No. 004-0221) and KC_{24} (JCPDS No. 019-0945) phases due to the intercalation of K-ion. The formation of these phases was further supported by the TEM analysis, as shown in Figure S6 (Supporting Information). The interlayer spacing of 0.097 and 0.304 nm corresponded to KC_8 (JCPDS No. 004-0221) and KC_{24} (JCPDS No. 019-0945) phases, respectively (Figure S6b and c, Supporting Information). Further proof of the intercalation of K-ions was provided by the high-angle annular dark-field (HAADF) image and the corresponding energy-dispersive X-ray spectroscopy (EDS) mappings, which indicated that K and C were distributed homogeneously in the sample matrix.

To better elucidate the reaction mechanism, we performed XPS analysis on the OPDMC-1000 electrode after it was discharged to 0.01 V vs. K/K^+ and charged to 2.0 V vs. K/K^+ , as shown in Figure 8. Compared with the pristine OPDMC-1000 electrode before the test (Figure 2b), the C1s peaks were significantly different after discharge, indicating the formation of the K-C material. To verify the formation of K-intercalation compounds, the C1s spectrum was deconvoluted. This yielded four peaks at 282.6, 284.6, 2385.5, and 288 eV, corresponding to KC_x , $C=C$, $C-OH$, and $C-COOH$ functional groups, respectively. Before the K-intercalation, no $K2p^{3/2}$ or $K2p^{1/2}$ peaks were

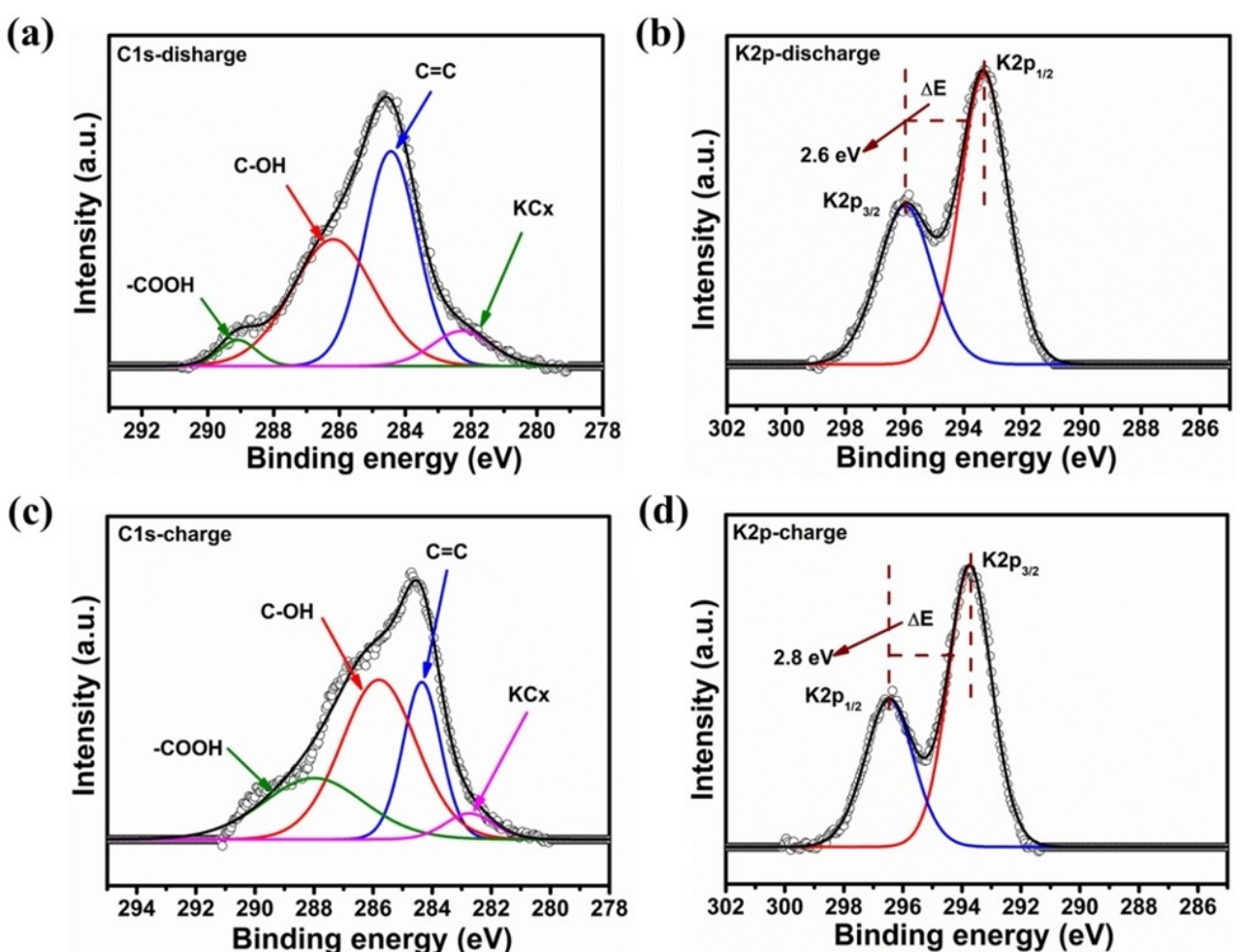


Figure 8. XPS spectra for the OPDMC-1000 electrode in the a, b) discharged and c, d) charged states.

detected for the OPDMC-1000 electrode (Figure 2b). After the K-intercalation process, the K2p peaks were clearly observed, indicating the insertion of K-ions. After the subsequent charging, small K2p peaks were observed. This indicates that in the first intercalation process, K-ions intercalated into the OPDMC-1000 electrode, forming K-C compounds, and in the subsequent deintercalation process, a small fraction of intercalated K-ions remained in the OPDMC-1000 electrode (Figure 8c and d). This explains the irreversible loss of K-ions after the first cycle, which led to a low coulombic efficiency. Similar observations were reported in cases where graphite was used as an anode^[26,50] for PIBs. To verify the aforementioned findings, Raman spectroscopy analysis of the OPDMC-1000 electrode in the discharged and charged states was performed, as shown in Figure S7 (Supporting Information). The intensity ratio of the D-band to the G-band in the Raman spectra indicated the degree of graphitisation for the carbonaceous materials. After the discharge process, the I_D/I_G ratio decreased from 1.04 to 0.977 as the potential decreased to 0.01 V vs. K/K⁺, indicating an increase in the degree of graphitisation. In the subsequent charge process, the I_D/I_G ratio increased from 0.977 to 0.983 as the potential increased from 0.01 to 2.0 V vs. K/K⁺, indicating a

decrease in the degree of graphitisation.^[46,50,51] After the charge cycle, the value of I_D/I_G did not recover to that of the pristine OPDMC-1000 electrode, indicating a higher degree of order for the discharged OPDMC-1000 electrode compared with the pristine OPDMC-1000 electrode.

2.4. Electrochemical Performance of Full Cell

Little information is available in the literature on the electrochemical performance of K-ion full cells, and the practical applicability of fabricated anodes has not been thoroughly investigated.^[52–57] This motivated us to investigate the practical applications of the high-performance OPDMC-1000 anode by assembling a full cell. The XRD pattern and morphology of commercial potassium Prussian blue used as cathode is shown in Figure S8 (Supporting Information). Before the full-cell assembly, the OPDMC-1000 anode was pre-potassiated by paring it with a K-metal to form a stable SEI layer. The K-ion full cell was assembled by coupling the OPDMC-1000 anode with a Prussian blue cathode ($KFe[Fe(CN)₆]$). Figure 9a shows the K-ion conduction between the OPDMC-1000 anode and $KFe[Fe(CN)₆]$

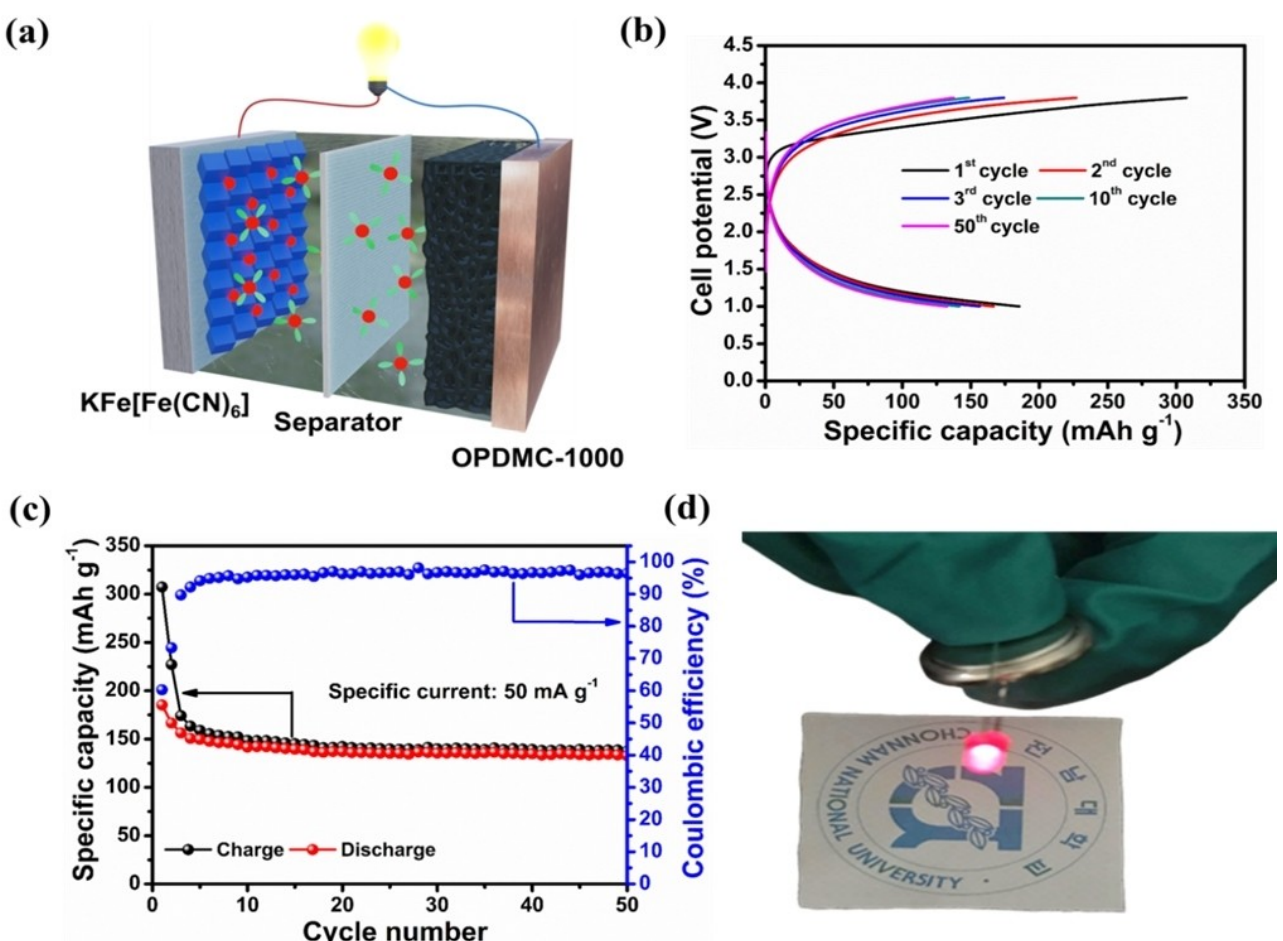


Figure 9. Electrochemical performance of the full cell comprising the OPDMC-1000 anode and $KFe[Fe(CN)₆]$ cathode. a) Schematic of the full cell. b) Galvanostatic charge/discharge potential profiles at a specific current of 50 mA g^{-1} . c) Cyclability at a specific current of 50 mA g^{-1} . d) Optical image showing the glowing red LED connected to the full cell.

cathode during the K-ion intercalation/deintercalation. Figure 9b shows the charge/discharge potential profile of the full cell at a specific current of 50 mA g^{-1} in the cell potential range of 1.0–3.8 V. The full cell exhibited impressive initial charge and discharge capacities of 307.40 and $185.32 \text{ mAh g}^{-1}$, respectively, and retained a capacity of $137.55 \text{ mAh g}^{-1}$ even after 50 cycles with a coulombic efficiency of 96.45% (Figure 9c). In addition, the rate capability of the full cell is presented in Figure S9. The full cell exhibited the reversible discharge capacities of 236.6, 156.2, 121, 88.3, 64.4, 41.2, and 26.3 mAh g^{-1} at increasing current densities of 30, 50, 100, 150, 200, 250, and 300 mA g^{-1} , respectively. When the current density returned to 30 mA g^{-1} , the reversible discharge capacity was recovered to 217 mAh g^{-1} , indicating a good rate performance of the full cell. Further, a red light-emitting diode (LED) was successfully lit when it was connected to the fabricated full cell, indicating that our fabricated cell can function effectively after being completely charged (Figure 9d). The energy density was calculated based on the total weight of the OPDMC-1000 anode and KFe[Fe(CN)₆] cathode. As shown Figure 9b, OPDMC-1000/KFe[Fe(CN)₆] full-cell, delivers a capacity of $137.55 \text{ mAh g}^{-1}$ with an average cell potential of 2.3 V after 50 cycles, which corresponds to an energy density of 63.3 Wh kg^{-1} . Thus, the suitability of the OPDMC-1000 anode in full cell assures the practical application of OPDMC electrode from waste orange peel in PIBs.

3. Conclusions

The scalable synthesis of 3D interconnected orange peel-derived mesoporous carbon (OPDMC) without using a chemical activating agent was performed, and the OPDMC was used as a high-performance anode material in potassium-ion batteries (PIBs) for the first time. XRD, Raman spectroscopy, TEM, and XPS analyses revealed the formation of turbostratic carbon upon heating of the OP in an inert atmosphere. Morphological and porosity evaluations indicated the evolution of a well-defined 3D interconnected mesoporous structure having an enhanced porosity and pore volume with increasing carbonisation temperature. The OPDMC-1000 sample exhibited better electrochemical properties, in terms of capacity, coulombic efficiency, cyclability, and rate performance, than did OPDMC-700 and OPDMC-500 samples when used as an anode in PIBs. According to the detailed characterisation, the ameliorative electrochemical performance of the OPDMC-1000 electrode is attributed to the combined contributions of the turbostratic structure with enlarged interlayer spacing, presence of abundant sp² domains, O-containing functional groups, and well-defined interconnected 3D porosity, which improved the electronic and ionic conductivities, allowed the accommodation of more K-ions, and suppressed the volume expansion. The OPDMC-1000 electrode exhibited initial discharge and charge capacities of 408 and 224 mAh g^{-1} , respectively, corresponding to an impressive coulombic efficiency of 55%. It retained a high capacity of 208.57 mA g^{-1} after 100 cycles at 30 mA g^{-1} . Furthermore, the OPDMC-1000 electrode exhibited long-term

cycling performance at high specific currents of 200 and 500 mA g^{-1} . As expected, it exhibited impressive cycling stability, maintaining reversible capacities of 150.37 and 112 mA g^{-1} after 2000 and 3000 cycles, respectively, which corresponds to a coulombic efficiency of near 100%. Furthermore, a full cell exhibited a superior reversible discharge capacity of $185.32 \text{ mAh g}^{-1}$ in the first cycle and a capacity retention of 71.60% after 50 cycles. The results of this study not only suggest the possibility of developing OPDMC as a potential anode material for KIBs but also provide a novel approach for designing cost-effective and ecofriendly electrode materials for energy-storage devices.

Experimental Section

Synthesis of orange peel derived mesoporous carbon (OPDMC)

The biowaste orange peel (OP) was collected from Jeju fruit and juice shops in South Korea. The collected biowaste OP was first washed with deionised (DI) water several times and dried at 85°C for 24 h in a vacuum oven. Then, the dried OP was crushed using a mortar and pestle to obtain yellow fine OP powder. The OP powder was carbonised at various temperatures (500, 700, and 1000°C) under an Ar flow of 100 sccm for 2 h at a heating rate of 5°C min^{-1} . The resulting black powder was immersed in a 2 M HCl (Sigma-Aldrich) solution to remove the metal impurities and finally washed with DI water several times, followed by drying at 85°C in the vacuum oven. The final obtained OPDMCs are denoted as OPDMC-500, OPDMC-700, and OPDMC-1000, corresponding to the carbonisation temperatures of 500, 700, and 1000°C , respectively.

Material characterisation

The structures of the OPDMC sample were characterised via 3D high-resolution X-ray diffractometer (XRD: 3D/MAX Ultima III, Rigaku) with a Cu-K α source (1.8 kW, Max. 60 kV, and 55 mA). To characterise the morphology and microstructure of the OPDMC sample, scanning electron microscopy (SEM: S-4700/EX-200, Hitachi) at an accelerating voltage of 10 kV and transmission electron microscopy (TEM: JEM-2100F, JEOL) at an accelerating voltage of 200 kV were used. The surface area and pore size of the OPDMC sample were characterised using a Brunauer-Emmett-Teller (BET: ASAP 2020, Micromeritics) analyser. Raman spectroscopy (NRS-5100, JASCO) with an excitation wavelength of 532 nm was used to investigate the chemical structure of the carbon compound formed upon heating of the OP. Additionally, the chemical composition, effect of the heating temperature on the chemical structure of the carbonaceous materials, and extent of reduction were investigated via X-ray photoelectron spectroscopy (XPS: MultiLab 2000, VG). The high-resolution XPS spectra were deconvoluted using the CASA XPS software with a Gaussian:Lorentzian ratio of 70:30. Prior to curve fitting, the background was subtracted from each spectrum via the Shirley method. The binding-energy position of 284.6 eV for C1s was used as a reference for peak calibration.

Electrochemical characterisation

Electrochemical characterisation was performed using a 2032-type coin cell. The OPDMC working electrode was assembled with K-metal as the counter and reference electrodes and a glass fibre separator(Whatman[®]) soaked with 0.75 M KPF₆ in ethylene

carbonate (EC) and dimethyl carbonate (DMC) (1:1 by volume), in an Ar-filled glovebox. The OPDMC powder was mixed with carbon black as a conductive agent and carboxymethyl cellulose (CMC) as a binder, at a weight ratio of 80:10:10. DI water, as a solvent, was used to obtain a uniform slurry. Then, the slurry was cast onto Cu foil, followed by drying at 85 °C overnight in a vacuum oven. The electrodes were punched into 14-mm-diameter disks. The mass loading of the anode was controlled at ~1.3 mg cm⁻². The OPDMC electrode was discharged and charged in the potential range of 0.01–2 V vs. K/K⁺ using an automatic battery cycler (WonATech-WBCS 3000). Furthermore, the electrochemical impedance of the cells was tested using a potentiostat/EIS (Gamry-PC750) in the frequency range of 10 mHz–100 KHz. For the XRD, TEM, XPS, and Raman spectroscopy analyses of the electrode, the cell was discharged/charged within a potential range of 0.01–2 V vs. K/K⁺ and then disassembled inside the glove box. Subsequently, the electrode was washed with the DMC solvent and dried at ~20 °C in the vacuum chamber of the glove box.

The coin type full cell composed of an OPDMC-1000 anode and a KFe[Fe(CN)₆] cathode was fabricated. The Prussian blue (KFe[Fe(CN)₆], Sigma-Aldrich) cathode was mixed with carbon black as a conductive agent and polyvinylidene difluoride (PVDF) as a binder, at a weight ratio of 70:20:10. An N-methyl-2-pyrrolidone solvent was used to obtain a homogeneous slurry. Then, the slurry was cast onto Al foil, followed by drying at 85 °C overnight in a vacuum oven. The cathode-to-anode loading Mass ratio was approximately 4:1. Galvanostatic charge/discharge tests were conducted in the cell potential range of 1.0–3.8 V.

Acknowledgements

This work was supported by National Research Foundation of Korea (NRF) grants (Nos. 2019R1A2C1084020 and 2018R1A5A1025224). It was also funded by the EES Technology Development Program (No. 20172420108730) through KETEP, Korea.

Conflict of Interest

The authors declare no conflict of interest.

Keywords: potassium-ion batteries • 3D interconnected mesoporous carbon • biomass • cyclability • full cell

- [1] Y. Liu, Z. Tai, T. Zhou, V. Sencadas, J. Zhang, L. Zhang, K. Konstantinov, Z. Guo, H. K. Liu, *Adv. Mater.* **2017**, *29*, 1703028.
- [2] L. X. Yuan, Z. H. Wang, W. X. Zhang, X. L. Hu, J. T. Chen, Y. H. Huang, J. B. Goodenough, *Energy Environ. Sci.* **2011**, *4*, 269–284.
- [3] H. Kim, J. C. Kim, M. Bianchini, D. H. Seo, J. Rodriguez-Garcia, G. Ceder, *Adv. Energy Mater.* **2018**, *8*, 1702384.
- [4] M. C. Lin, M. Gong, B. Lu, Y. Wu, D. Y. Wang, M. Guan, M. Angell, C. Chen, J. Yang, B. J. Hwang, H. Dai, *Nature* **2015**, *520*, 325–328.
- [5] N. Singh, T. S. Arthur, C. Ling, M. Matsui, F. Mizuno, *Chem. Commun.* **2013**, *49*, 149–151.
- [6] N. Yabuuchi, K. Kubota, M. Dahbi, S. Komaba, *Chem. Rev.* **2014**, *114*, 11636–11682.
- [7] W. Zhang, J. Mao, S. Li, Z. Chen, Z. Guo, *J. Am. Chem. Soc.* **2017**, *139*, 3316–3319.
- [8] K. Kubota, M. Dahbi, T. Hosaka, S. Kumakura, S. Komaba, *Chem. Rec.* **2018**, *18*, 459–479.
- [9] J. Y. Hwang, S. T. Myung, Y. K. Sun, *Adv. Funct. Mater.* **2018**, *28*, 1802938.
- [10] A. Eftekhari, Z. Jian, X. Ji, *ACS Appl. Mater. Interfaces* **2017**, *9*, 4404–4419.
- [11] S. R. Taylor, *Geochim. Cosmochim. Acta* **1964**, *28*, 1273–1285.
- [12] S. Komaba, T. Hasegawa, M. Dahbi, K. Kubota, *Electrochim. Commun.* **2015**, *60*, 172–175.
- [13] Y. Hamon, T. Brousse, F. Jousse, P. Topart, P. Buvat, D. M. Schleich, *J. Power Sources* **2001**, *97*–98, 185–187.
- [14] L. Fan, Q. Liu, S. Chen, K. Lin, Z. Xu, B. Lu, *Small* **2017**, *13*, 1701011.
- [15] K. Beltrop, S. Beuker, A. Heckmann, M. Winter, T. Placke, *Energy Environ. Sci.* **2017**, *10*, 2090–2094.
- [16] J. Zhu, Y. Li, B. Yang, L. Liu, J. Li, X. Yan, D. He, *Small* **2018**, *14*, 1801836.
- [17] B. Ji, F. Zhang, N. Wu, Y. Tang, *Adv. Energy Mater.* **2017**, *7*, 1700920.
- [18] V. Gabaudan, L. Monconduit, L. Stievano, R. Berthelot, *Front. Energy Res.* **2019**, *7*, 1–16.
- [19] R. Verma, P. N. Didwal, H.-S. Ki, G. Cao, C.-J. Park, *ACS Appl. Mater. Interfaces* **2019**, *11*, 26976–26984.
- [20] D. S. Bin, S. Y. Duan, X. J. Lin, L. Liu, Y. Liu, Y. S. Xu, Y. G. Sun, X. Sen Tao, A. M. Cao, L. J. Wan, *Nano Energy* **2019**, *60*, 912–918.
- [21] V. Gabaudan, R. Berthelot, L. Stievano, L. Monconduit, *ACS Omega* **2018**, *3*, 12195–12200.
- [22] H. Gao, T. Zhou, Y. Zheng, Q. Zhang, Y. Liu, J. Chen, H. Liu, Z. Guo, *Adv. Funct. Mater.* **2017**, *27*, 1702634.
- [23] Z. Jian, Z. Xing, C. Bommier, Z. Li, X. Ji, *Adv. Energy Mater.* **2016**, *6*, 1501874.
- [24] Z. Ju, S. Zhang, Z. Xing, Q. Zhuang, Y. Qiang, Y. Qian, *ACS Appl. Mater. Interfaces* **2016**, *8*, 20682–20690.
- [25] X. Zhao, P. Xiong, J. Meng, Y. Liang, J. Wang, Y. Xu, *J. Mater. Chem. A* **2017**, *5*, 19237–19244.
- [26] Z. Jian, W. Luo, X. Ji, *J. Am. Chem. Soc.* **2015**, *137*, 11566–11569.
- [27] X. Zou, P. Xiong, J. Zhao, J. Hu, Z. Liu, Y. Xu, *Phys. Chem. Chem. Phys.* **2017**, *19*, 26495–26506.
- [28] Q. Gan, J. Xie, Y. Zhu, F. Zhang, P. Zhang, Z. He, S. Liu, *ACS Appl. Mater. Interfaces* **2019**, *11*, 930–939.
- [29] J. Li, W. Qin, J. Xie, H. Lei, Y. Zhu, W. Huang, X. Xu, Z. Zhao, W. Mai, *Nano Energy* **2018**, *53*, 415–424.
- [30] M. Chen, W. Wang, X. Liang, S. Gong, J. Liu, Q. Wang, S. Guo, H. Yang, *Adv. Energy Mater.* **2018**, *8*, 1800171.
- [31] J. Ruan, X. Wu, Y. Wang, S. Zheng, D. Sun, Y. Song, M. Chen, *J. Mater. Chem. A* **2019**, *7*, 19305–19315.
- [32] W. Yang, J. Zhou, S. Wang, W. Zhang, Z. Wang, F. Lv, K. Wang, Q. Sun, S. Guo, *Energy Environ. Sci.* **2019**, *12*, 1605–1612.
- [33] D. Li, X. Ren, Q. Ai, Q. Sun, L. Zhu, Y. Liu, Z. Liang, R. Peng, P. Si, J. Lou, J. Feng, L. Ci, *Adv. Energy Mater.* **2018**, *8*, 1802386.
- [34] W. Cao, E. Zhang, J. Wang, Z. Liu, J. Ge, X. Yu, H. Yang, B. Lu, *Electrochim. Acta* **2019**, *293*, 364–370.
- [35] X. He, J. Liao, Z. Tang, L. Xiao, X. Ding, Q. Hu, Z. Wen, C. Chen, *J. Power Sources* **2018**, *396*, 533–541.
- [36] Y. Li, R. A. Adams, A. Arora, V. G. Pol, A. M. Levine, R. J. Lee, K. Akato, A. K. Naskar, M. P. Paranthaman, *J. Electrochem. Soc.* **2017**, *164*, A1234–A1238.
- [37] C. Gao, Q. Wang, S. Luo, Z. Wang, Y. Zhang, Y. Liu, A. Hao, R. Guo, *J. Power Sources* **2019**, *415*, 165–171.
- [38] L. Jiang, L. Sheng, Z. Fan, *Sci. China Chem.* **2018**, *61*, 133–158.
- [39] J. Wang, P. Nie, B. Ding, S. Dong, X. Hao, H. Dou, X. Zhang, *J. Mater. Chem. A* **2017**, *5*, 2411–2428.
- [40] L. A. Pfaltzgraff, M. De Bruyn, E. C. Cooper, V. Budarin, J. H. Clark, *Green Chem.* **2013**, *15*, 307–314.
- [41] H. A. A. El-aal, F. T. Halawehish, *Lucr. Stiint.* **2012**, *53*, 233–240.
- [42] C. K. Ranaweera, P. K. Kahol, M. Ghimire, S. R. Mishra, R. K. Gupta, *C* **2017**, *3*, 25.
- [43] M. Mahajan, M. Ulaganathan, V. Aravindan, S. Sreejith, Q. Yan, S. Madhavi, J. Y. Wang, T. M. Lim, *ChemistrySelect* **2017**, *2*, 5051–5058.
- [44] A. C. Ferrari, J. Robertson, *Phy. Rev. B* **2000**, *61*, 14095–14107.
- [45] A. Ganguly, S. Sharma, P. Papakonstantinou, J. Hamilton, *J. Phys. Chem. C* **2011**, *115*, 17009–17019.
- [46] L. Liu, Y. Chen, Y. Xie, P. Tao, Q. Li, C. Yan, *Adv. Funct. Mater.* **2018**, *28*, 1801989.
- [47] Z. Jian, Z. Xing, C. Bommier, Z. Li, X. Ji, *Adv. Energy Mater.* **2016**, *6*, 1501874.
- [48] G. Wang, X. Xiong, D. Xie, Z. Lin, J. Zheng, F. Zheng, Y. Li, Y. Liu, C. Yang, M. Liu, *J. Mater. Chem. A* **2018**, *6*, 24317–24323.
- [49] Y. Lei, L. Qin, R. Liu, K. C. Lau, Y. Wu, D. Zhai, B. Li, F. Kang, *ACS Appl. Energy Mater.* **2018**, *1*, 1828–1833.

- [50] W. Wang, J. Zhou, Z. Wang, L. Zhao, P. Li, Y. Yang, C. Yang, H. Huang, S. Guo, *Adv. Energy Mater.* **2018**, *8*, 1701648.
- [51] G. Xia, C. Wang, P. Jiang, J. Lu, J. Diao, Q. Chen, *J. Mater. Chem. A* **2019**, *7*, 12317–12324.
- [52] Y. Xu, C. Zhang, M. Zhou, Q. Fu, C. Zhao, M. Wu, Y. Lei, *Nat. Commun.* **2018**, *9*, 1720.
- [53] X. Wang, K. Han, D. Qin, Q. Li, C. Wang, C. Niu, L. Mai, *Nanoscale* **2017**, *9*, 18216–18222.
- [54] S. Chong, Y. Wu, C. Liu, Y. Chen, S. Guo, Y. Liu, G. Cao, *Nano Energy* **2018**, *54*, 106–115.
- [55] Y. Xie, Y. Chen, L. Liu, P. Tao, M. Fan, N. Xu, X. Shen, C. Yan, *Adv. Mater.* **2017**, *29*, 1702268.
- [56] C. Lv, W. Xu, H. Liu, L. Zhang, S. Chen, X. Yang, X. Xu, D. Yang, *Small* **2019**, *15*, 1900816.
- [57] L. Fan, R. Ma, Q. Zhang, X. Jia, B. Lu, *Angew. Chem. Int. Ed.* **2019**, *58*, 10500–10505.
- [58] W. Luo, J. Wan, B. Ozdemir, W. Bao, Y. Chen, J. Dai, H. Lin, Y. Xu, F. Gu, V. Barone, L. Hu, *Nano Lett.* **2015**, *15*, 7671–7677.
- [59] J. Zhao, X. Zou, Y. Zhu, Y. Xu, C. Wang, *Adv. Funct. Mater.* **2016**, *26*, 8103.
- [60] C. Chen, Z. Wang, B. Zhang, L. Miao, J. Cai, L. Peng, Y. Huang, J. Jiang, Y. Huang, L. Zhang, J. Xie, *Energy Storage Mater.* **2017**, *8*, 161–168.
- [61] B. Cao, Q. Zhang, H. Liu, B. Xu, S. Zhang, T. Zhou, J. Mao, W. K. Pang, Z. Guo, A. Li, J. Zhou, X. Chen, H. Song, *Adv. Energy Mater.* **2018**, *8*, 1801149.
- [62] K. Share, A. P. Cohn, R. E. Carter, C. L. Pint, *Nanoscale* **2016**, *8*, 16435.
- [63] H. Li, Z. Cheng, Q. Zhang, A. Natan, Y. Yang, D. Cao, H. Zhu, *Nano Lett.* **2018**, *18*, 7407.
- [64] X. Wu, C. W. K. Lam, N. Wu, S.-S. Pang, Z. Xing, W. Zhang, Z. Ju, *Mater. Today* **2019**, *11*, 182–191.
- [65] W. Luo, J. Wan, B. Ozdemir, W. Bao, Y. Chen, J. Dai, H. Lin, Y. Xu, F. Gu, V. Barone, L. Hu, *Nano Lett.* **2015**, *15*, 7671–7677.

Manuscript received: April 1, 2020

Revised manuscript received: May 13, 2020

Accepted manuscript online: June 3, 2020

Version of record online: June 30, 2020